View metadata, citation and similar papers at core.ac.uk

brought to you by CORE

provided by Elsevier - Publisher Connector

Journal of High Energy Astrophysics 1–2 (2014) 63–70

Contents lists available at ScienceDirect

Journal of High Energy Astrophysics

www.elsevier.com/locate/jheap

Time dependent leptonic modeling of Fermi II processes in the jets of flat spectrum radio quasars

C. Diltz [a], M. Böttcher [b,a,*]

[a] Astrophysical Institute, Department of Physics and Astronomy, Ohio University, Athens, OH 45701, USA
[b] Centre for Space Research, North-West University, Potchefstroom, 2520, South Africa

ARTICLE INFO

Article history:
Received 11 March 2014
Accepted 10 April 2014

Keywords:
Active and peculiar galaxies and related systems
γ-rays
Radiative transfer
Elementary particle processes

ABSTRACT

In this paper, we discuss the light-curve features of various flaring scenarios in a time-dependent leptonic model for low-frequency-peaked blazars. The quasar 3C273 is used as an illustrative example. Our code takes into account Fermi-II acceleration and all relevant electron cooling terms, including the external radiation fields generally found to be important in the modeling of the SEDs of FSRQs, as well as synchrotron self absorption and $\gamma\gamma$ pair-production. General parameters are constrained through a fit to the average spectral energy distribution (SED) of the blazar by numerically solving the time-dependent Fokker–Planck equation for the electron evolution in a steady-state situation. We then apply perturbations to several input parameters (magnetic field, particle injection luminosity, acceleration time scale) to simulate flaring events and compute time-dependent SEDs and light curves in representative energy bands (radio, optical, X-rays, γ-rays). Time lags between different bands are evaluated using a discrete cross correlation analysis. We find that Fermi-II acceleration has a significant effect on the distributions and that flaring events caused by increased acceleration efficiency of the Fermi II process will produce a correlation between the radio, optical and γ-ray bandpasses, but an anti-correlation between these three bandpasses and the X-ray band, with the X-rays lagging behind the variations in other bands by up to several hours.

© 2014 Elsevier B.V. All rights reserved.

1. Introduction

Blazars represent a class of radio-loud Active Galactic Nuclei that consists of BL Lac objects and Flat Spectrum Radio Quasars (FSRQs). The spectral energy distributions (SED) of blazars is characterized by two broadband, nonthermal components that span from the radio to UV or X-ray wavelengths and from X-rays to high-energy γ-rays. The extreme inferred isotropic-equivalent γ-ray luminosities, combined with rapid variability in different bandpasses, in some cases, down to just a few minutes, provides evidence for strong Doppler boosting in these sources. This is considered to be the result of beamed emission from relativistic jets closely aligned with our line of sight. It is generally accepted that the low-energy spectral component is synchrotron emission of relativistic electrons/positrons. For the origin of the high-energy SED component, two different approaches have been discussed, referred to as leptonic and hadronic models (for a review of both types of models, see, e.g., Böttcher, 2007; Böttcher et al., 2012). In the leptonic scenario, the X-ray to γ-ray emission is due to the inverse Compton scattering off the relativistic electrons, with the target photon fields either being the synchrotron photons within the emission region (SSC = synchrotron self Compton), or photons external to the jet (EC = external Compton). The external photon fields can include the accretion disk (Dermer et al., 1992; Dermer and Schlickeiser, 1993), the broad line region (BLR), (Sikora et al., 1994; Blandford and Levinson, 1995), or even an infrared emitting dust torus (IR) that surrounds the central accretion flow onto supermassive black hole (Blazejowski et al., 2000). Leptonic models are widely used and have been relatively successful in modeling the SEDs and some variability features of blazars. In hadronic models (e.g., Mannheim and Biermann, 1992; Mastichiadis and Kirk, 1995, 2005; Mücke and Protheroe, 2001; Mücke et al., 2003; Böttcher et al., 2013), γ-rays are the result of proton synchrotron radiation as well as π^0-decay and synchrotron and Compton radiation from secondary particles in photo-pion induced cascades, presuming the existence of ultra-relativistic protons in the emission region. While such models have also had success in modeling the SEDs of blazars and remain viable, rapid variability observed in blazars is more readily explained in terms of the much shorter acceleration and cooling time scales of relativistic leptons. Therefore, in this work, we will focus on leptonic models.

* Corresponding author at: Centre for Space Research, North-West University, Potchefstroom, 2520, South Africa.

http://dx.doi.org/10.1016/j.jheap.2014.04.001
2214-4048/© 2014 Elsevier B.V. All rights reserved.

The shapes of the spectral components provide insight into the underlying particle distribution that is producing the emission. Simple power-law and broken power-law electron distributions with parameters chosen ad-hoc, have often been invoked in order to model the SEDs of blazars. Alternatively, log-parabolic electron distributions have been successfully employed to produce the curved synchrotron and Compton spectra observed in many blazars (Massaro et al., 2006a, 2006b; Cerruti et al., 2013; Dermer et al., 2014). The log-parabola function is characterized by two variables that describe the spectral parameter of the electron distribution and the spectral curvature of the distribution. The log parabolic shape has been shown to be analytically related to a stochastic acceleration mechanism, in which the acceleration probability decreases with energy (Rani et al., 2011; Massaro et al., 2006a, 2006b). Such a connection of log-parabolic spectra and acceleration mechanisms naturally arises in solutions of the time dependent Fokker–Planck equation that contains a momentum diffusion term, indicative of Fermi II acceleration, when the evolution reaches equilibrium (Tramacere et al., 2011; Massaro et al., 2006b). They showed that the spectral curvature is inversely proportional to the momentum diffusion coefficient, since the diffusion term acts to broaden the shape of the particle distribution.

Second order Fermi acceleration is therefore a viable mechanism for producing log-parabola particle spectra which may be hard enough to reproduce the hard spectra of γ-ray emission observed in several TeV blazars (Lefa et al., 2011; Asano et al., 2013). It has also been shown that relativistic Maxwellian electron distributions can result from stochastic acceleration processes balanced by radiative losses (Schlickeiser, 1984a). For the full time dependent Fokker–Planck equation incorporating Fermi II acceleration, general solutions have been found using Green's functions and the application of spectral operators (Stawarz and Petrosian, 2008; Tramacere et al., 2011). Solutions to the Fokker–Planck equation incorporating both Fermi I and Fermi II processes, have been developed for the application of the transport of energetic ions (Becker and Dermer, 2006). Solutions have also been obtained that consider both Fermi I and Fermi II acceleration, and radiative losses in the Thomson regime (Schlickeiser, 1984a, 1984b). However, when Klein–Nishina effects on the electron cooling rates, as well as absorption processes in the radiation transfer problem, are taken into account, one needs to resort to numerical solutions of the Fokker–Planck equation. Asano et al. (2013) developed a time dependent Leptonic model that incorporated Fermi II processes to study the hard spectrum of the blazars Mrk 421 and 1ES 1101-232. The curvature of the electron spectrum, as well as the hard γ-ray spectra could be reproduced by a model that utilizes a stochastic momentum diffusion process (Fermi II).

In this paper, we use a time-dependent Leptonic model that incorporates Fermi acceleration and self-consistent radiative losses, including synchrotron and Compton scattering on internal (SSC) and external (EC) radiation fields as well as synchrotron self-absorption and $\gamma\gamma$ absorption and pair production. The purpose of this paper is to investigate the effects of various flaring scenarios, including Fermi-II acceleration, in external-Compton dominated blazars to complement the study for SSC-dominated sources by Asano et al. (2013). Therefore, while our code is applicable to all types of blazars, we here focus on its application to FSRQs. We describe the model and underlying assumptions in Section 2. We use our code to study the influence of Fermi-II acceleration on the quasi-equilibrium particle distribution and light-curve features, including possible time delays between variations in different frequency bands. These features are studied with parameters motivated by an SED fit to the FSRQ 3C273, described in Section 3. Once we have obtained appropriate baseline parameters, we choose a set of input parameters (specifically, the particle injection luminosity, the magnetic field, and the acceleration time scale) to perturb them in the form of a Gaussian in time, in order to study the light curves in the radio, optical, X-ray and γ-ray bandpasses (Section 4). In Section 5, we perform a discrete correlation function analysis on the light curves obtained in the preceding section, to determine possible time lags between the selected bandpasses. We summarize and discuss our results in Section 6. Throughout this paper, a cosmology with $\Omega_m = 0.3$, $\Omega_\Lambda = 0.7$, and $H_0 = 70$ km s^{-1} Mpc^{-1} is used.

2. Model setup

Our model is based on a single, homogeneous emission region of radial size R which moves relativistically with bulk Lorentz factor Γ along a pre-existing jet structure, oriented at a small angle $\theta_{\rm obs}$ with respect to our line of sight. Throughout the paper, unprimed quantities denote values in the co-moving frame of the emission region, while primed quantities denote values in the stationary AGN frame. The emission region is pervaded by a homogeneous, randomly oriented magnetic field of strength B. The size of the emission region is constrained by the observed variability time scale, Δt, through

$$R = \frac{c \cdot \Delta t \cdot \delta}{1+z} \tag{1}$$

where z is the redshift to the source and $\delta = (\Gamma[1-\beta_\Gamma \cos\theta_{\rm obs}])^{-1}$ is the Doppler factor.

A population of an ultra-relativistic electrons is continuously injected. We assume that the electron injection spectrum is in the form of a power-law distribution with the functional form

$$Q(\gamma, t) = Q_0(t)\gamma^{-q} H(\gamma; \gamma_{\rm min}, \gamma_{\rm max}) \tag{2}$$

where $H(\gamma; \gamma_{\rm min}, \gamma_{\rm min})$ denotes the Heaviside function defined by $H = 1$ if $\gamma_{\rm min} \le \gamma \le \gamma_{\rm max}$, and $H = 0$ otherwise. The normalization factor for the injection spectrum is determined through the injection luminosity by

$$Q_0 = \begin{cases} \frac{L_{\rm inj}(t)}{V_b m_e c^2} \frac{2-q}{\gamma_2^{2-q} - \gamma_1^{2-q}} & \text{if } q \neq 2, \\ \frac{L_{\rm inj}(t)}{V_b m_e c^2 \ln(\frac{\gamma_2}{\gamma_1})} & \text{if } q = 2, \end{cases} \tag{3}$$

where V_b denotes the co-moving blob of the emission region and m_e denotes the rest mass of an electron.

The time evolution of the electron distribution is found by numerically solving the time-dependent Fokker–Planck equation, which is given in the following form:

$$\frac{\partial n_e(\gamma,t)}{\partial t} = \frac{\partial}{\partial \gamma}\left[\frac{1}{(a+2)\cdot t_{\rm acc}} \cdot \gamma^2 \cdot \frac{\partial n_e(\gamma,t)}{\partial \gamma}\right] - \frac{\partial}{\partial \gamma}\left(\dot{\gamma}_{\rm rad} \cdot n_e(\gamma,t)\right) + Q(\gamma,t) - \frac{n_e(\gamma,t)}{t_{\rm esc}} \tag{4}$$

where $a = v_s^2/v_A^2$, v_A represents the Alfven velocity, v_s represents the shock velocity. In this study, a value of $a = 10^{-3}$ is chosen. $\dot{\gamma}_{\rm rad}$ denotes the radiative (synchrotron and Compton) losses, taking into account Klein–Nishina effects (e.g., Böttcher et al., 1997). Synchrotron losses are governed by the strength of the randomly oriented magnetic field within the emission region. Inverse Compton losses are governed by the scattering of the electrons with the synchrotron photons that they produce (SSC) or by the external radiation fields surrounding the black hole (EC). These radiation fields include emission directly from the accretion disk, emission reprocessed by the Broad Line Region (BLR), and radiation emitted by a dusty torus.

In addition to radiative losses, the electron distribution is subjected gyro-resonant wave–particle interactions with hydromagnetic turbulence described by a turbulent plasma wave spectrum

$I(k) \propto k^{-p}$ with index p, where k is the wave number of turbulent plasma waves.

If the energy density of the plasma waves is small compared to the energy density of the magnetic field (quasi-linear approximation), then the diffusion coefficient becomes a power law function of the form

$$D(\gamma) = K \cdot \gamma^{p} \tag{5}$$

In this work, we consider a diffusion coefficient with a spectral index $p = 2$ (hard sphere scattering). This makes the acceleration time scale independent of energy. The normalization of the diffusion coefficient is given by $K = 1/([a+2]t_{\rm acc})$. The values $t_{\rm acc}$ and t_{esc} represent the acceleration and escape time scales, respectively. We parameterize the escape time scale in terms of the light crossing time scale as $t_{\rm esc} = \eta R/c$ where $\eta \geq 1$.

The Fokker–Planck equation is solved through an implicit Crank–Nichelson scheme that converts the partial differential equation into a tri-diagonal set of linear equations. The solution to the linear equations is then found through a tri-diagonal matrix algorithm. This method has the advantage of being unconditionally stable, allowing us to use arbitrarily large time steps to numerically solve the partial differential equation when approaching equilibrium.

Simultaneously with the Fokker–Planck equation (4) for the electrons, we solve a separate evolution equation for the photon field in the emission region:

$$\frac{\partial n_{ph}(\nu,t)}{\partial t} = \frac{4\pi}{h\nu} \cdot j_{\nu}(t) - n_{ph}(\nu,t) \cdot \left(\frac{1}{t_{\rm esc,ph}} + \frac{1}{t_{\rm abs}} \right) \tag{6}$$

where j_{ν} denotes the emissivity due to the various radiation mechanisms, $t_{\rm esc,ph} = 4R/3c$ is the photon escape time scale and $t_{\rm abs}$ denotes the absorption time scale due to synchrotron self absorption and gamma–gamma absorption. The absorption time scale can be defined through the opacities τ, as

$$t_{\rm abs} = \frac{R}{c \cdot (\tau_{\rm SSA} + \tau_{\gamma\gamma})} \tag{7}$$

where τ_{SSA} and $\tau_{\gamma\gamma}$ denote the synchrotron-self-absorption and $\gamma\gamma$ absorption opacities. With the solution to the photon field at any given time step, we then compute the emerging (observable) broadband spectrum in the observer's frame through

$$f'_{\nu'}(t') \equiv \nu' F'_{\nu'}(t') = \frac{h \cdot \nu^2 \cdot n_{ph}(\nu,t) \cdot \delta^4 \cdot V_{co}}{4\pi d_L^2 \cdot t_{\rm esc,ph}} \tag{8}$$

At every time step, separate subroutines are used to compute the emission coefficients for the various radiation processes in the co-moving frame of the emission region. The synchrotron emission coefficient is evaluated as

$$j_{\nu,\rm syn}(t) = \frac{1}{4\pi} \int_0^{\infty} d\gamma n_e(\gamma,t) \cdot P_{\nu}(\gamma) \tag{9}$$

where the term $P_{\nu}(\gamma)$ denotes the spectral synchrotron power of a single lepton. The spectral synchrotron power is approximated by Böttcher et al. (2012):

$$P_{\nu}(\gamma) = \frac{32\pi c}{9\Gamma(4/3)} \cdot r_e^2 \left(\frac{m_e}{m} \right)^2 \cdot u_B \gamma^2 \cdot \frac{\nu^{1/3}}{\nu_c^{4/3}} e^{-\nu/\nu_c} \tag{10}$$

where u_B denotes the energy density of the magnetic field and r_e denotes the classical electron radius. The critical frequency for the synchrotron spectrum is $\nu_c = (4.2 \times 10^6 B(m_e/m)) \cdot \gamma^2$ Hz.

The SSC emissivity is calculated using the solution of Jones (1968) for Compton scattering of an isotropic radiation field by an isotropic distribution of relativistic electrons. Our code uses the entire co-moving photon field as targets for Compton scattering, thus incorporating higher-order SSC scattering.

For the external radiation field from the accretion disk, we assume that the disk is in the form of a Shakura–Sunyaev disk (Shakura and Sunyaev, 1973) with the following intensity profile:

$$I'^{SS}_{\epsilon}(\Omega'; \tilde{R}') = \frac{3GM\dot{m}}{16\pi^2 R^3} \cdot \varphi(\tilde{R}') \cdot \delta\left(\epsilon' - \frac{C}{\tilde{R}'^{3/4}} \right) \tag{11}$$

where $\epsilon' = h\nu'/m_e c^2$ is the photon energy normalized to the electron rest energy in the AGN frame and $\varphi(\tilde{R}')$ is defined by

$$\varphi(\tilde{R}') = 1 - \beta_i \cdot \left(R'_i/R' \right)^{1/2} \tag{12}$$

where β_i denotes the fraction of angular momentum captured by the black hole at the radius R_i, the innermost stable circular orbit around the black hole. The constant C is defined by

$$C = 1.51 \times 10^{-4} \left(\frac{l_{\rm edd}}{\eta_f M_9} \right)^{1/4} \tag{13}$$

and $\tilde{R}' = R'/R'_g$, with R'_g denoting the gravitational radius. With this representation for the intensity, we can compute the observed νF_{ν} flux of the accretion disk (Dermer and Menon, 2009):

$$f'_{\epsilon',SS} = \frac{l_{\rm edd} L_{\rm edd}}{2\pi d_L^2 \eta_f \tilde{R}'_{\rm min}} \cdot \left(\frac{\epsilon'}{\epsilon'_{\rm max}} \right)^{4/3} \cdot \exp\left(-\epsilon'/\epsilon'_{\rm max} \right) \tag{14}$$

We next consider an isotropic, external blackbody radiation field of temperature T_{BB} surrounding the emission region. This is an appropriate representation for a thermal IR radiation field from a dust torus (with $T_{bb} \lesssim 1000$ K), but also produces an external-Compton spectrum in good agreement with that resulting from a full BLR radiation field for $T_{bb} \sim$ a few 10^3 K (Böttcher et al., 2013), as long as the emission region is not located far beyond the outer boundary of the BLR. The spectral energy density of the external radiation field is

$$u'(\epsilon') = K \frac{\epsilon'^3}{\exp(\epsilon'/\Theta) - 1} \tag{15}$$

where K denotes the normalization constant and $\Theta = kT/(m_e c^2)$ denotes the dimensionless temperature parameter. The normalization constant is constrained equating $\int_0^{\infty} u'(\epsilon')\, d\epsilon'$ to the expected energy density of the radiation field in the AGN frame

$$u'_{\rm ext} = \frac{L'_d \tau}{4\pi R'^2_{\rm ext} c} \tag{16}$$

where L_d denotes the total luminosity of the disk and τ denotes the fraction of the disk's radiation that's reprocessed by either the dust torus or the BLR and reemitted as thermal radiation, and $R_{\rm ext}$ denotes the radius of the (assumed spherical) reprocessing material. In order to evaluate the emission coefficients for EC scattering in the co-moving frame, we need to transform the spectral energy density (Eq. (15)) from the AGN frame to the co-moving frame through (Dermer and Menon, 2009):

$$u(\epsilon, \Omega) = \frac{u'(\epsilon', \Omega')}{\Gamma^3 (1 + \beta\mu)^3} \tag{17}$$

where μ denotes the cosine of the angle between the normalized, negative bulk velocity of the emission region and direction of propagation of photons in the co-moving frame, and $u'(\epsilon', \Omega') = u'(\epsilon')/(4\pi)$ under the assumption of isotropy in the AGN rest frame. The resulting spectral energy density in the co-moving frame is then used to evaluate the emission coefficient in the co-moving frame.

For time dependent modeling, evaluating the full expressions for the EC emission coefficients, involving full integrations over the solid angles of the target photon field and the electron distributions in the co-moving frame, is impractically time-consuming. Therefore, in order to save computing time, we assume that photons from both the accretion disk and the isotropic radiation field are boosted into the relativistic blob in the forward direction, thus replacing the angular characteristic of Eq. (17) by a δ function $\delta(\mu+1)$. For the accretion disk, we invoke the near field approximation (Dermer and Menon, 2009), which is valid as long as the relativistic blob is near the black hole:

$$u_{\rm disk}(\epsilon,\Omega) = \frac{u_{NF}}{2\pi}\cdot\delta\left(\epsilon-\Gamma\epsilon'_*/2\right)\cdot\delta(\mu+1) \tag{18}$$

where u'_{NF} denotes the total energy density of the accretion disk in the near-field regime in the co-moving frame and ϵ'_* denotes the peak energy of the accretion-disk emission.

For the isotropic radiation field, we construct the energy density in the co-moving frame using

$$u_{\rm ext}(\epsilon,\Omega) = \frac{15u_{IR}}{2\pi^5(\Theta)^4}\cdot\frac{\epsilon^3}{\exp(\epsilon/\Theta)-1}\cdot\delta(\mu+1) \tag{19}$$

With Eqs. (18) and (19), we use the relations given in Dermer and Menon (2009) to compute the corresponding EC emission coefficients.

Once we have the combined photon field of all the radiation fields in the co-moving frame, we compute the $\gamma\gamma$ absorption opacity (Dermer and Menon, 2009), and the pair production rate (Böttcher and Schlickeiser, 1997). The produced pair spectrum is added to the solution of the Fokker–Planck equation from the current time step, and $\tau_{\gamma\gamma}$ is included in the calculation of the photon absorption time scale (Eq. (7)) for the next time step.

3. Steady state spectrum

The purpose of this paper is a generic study of variability features caused by variations of individual emission-region parameters in the model described in the previous section. To choose realistic baseline parameters for this study, we perform a fit to the time-averaged SED of the FSRQ 3C273 (data taken from Abdo et al., 2010), based on an equilibrium solution obtained with our code with time-independent input parameters. The equilibrium model is fully determined through the following list of input parameters: The magnetic field B, the observed variability time scale, $\Delta t_{\rm var}$, the bulk Lorentz factor Γ, the observing angle $\theta_{\rm obs}$, the low- and high-energy cutoffs $\gamma_{\rm min,max}$ and spectral index q of the electron injection spectrum, the electron injection luminosity $L_{\rm inj}$, the accretion disk luminosity $L'_{\rm disk}$, the initial distance of the emission region from the central black hole, $R_{\rm axis}$, the characteristic extent $R'_{\rm ext}$, energy density $u'_{\rm ext}$, and blackbody temperature $T_{\rm BB}$ of the external radiation field, and the ratio between the acceleration and escape time scales, $t_{\rm acc}/t_{\rm esc}$.

Several of these parameters may be either directly measured or constrained through observations. Specifically, for 3C273, we have the following observables (see Böttcher et al., 2013 for references to the observational data): $z=0.158$, $\beta_{\perp,\rm app}=13$ (the apparent transverse velocity of individual jet components, normalized to the speed of light), $\Delta t_{\rm var}\sim 1$ d, $L_{\rm disk}=1.3\times10^{47}$ erg s^{-1}, and $L_{\rm BLR}=9.1\times10^{45}$ erg s^{-1}. The observed apparent superluminal speed implies a limit to the bulk Lorentz factor of $\Gamma>13$. We choose the observing angle as $\theta_{\rm obs}=1/\Gamma$ so that $\delta=\Gamma$, and the size of the emission region is then constrained by Eq. (1). In the SED of 3C273, the accretion disk component is directly visible as a prominent Big Blue Bump, which facilitates reliable estimates of the black hole mass and Eddington ratio, $l_{\rm Edd}=L_{\rm disk}/L_{\rm Edd}$. The observed BLR luminosity is related to the disk luminosity through

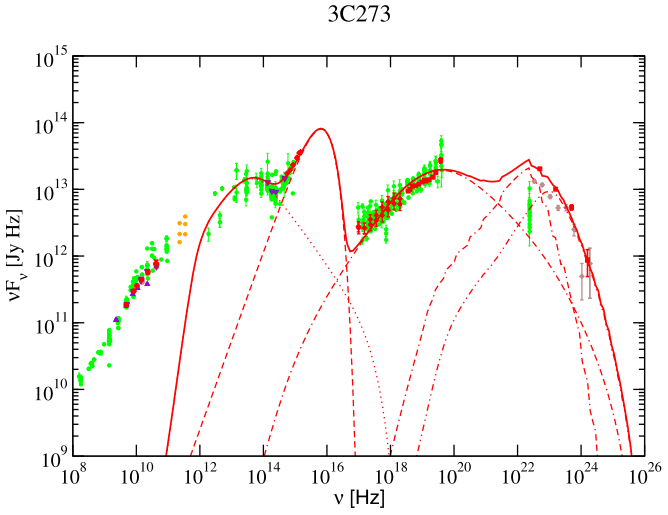

Fig. 1. Equilibrium fit to the time-averaged SED of 3C273. See Table 1 for parameter values. The line styles denote: solid = overall fit, dotted = synchrotron, dashed = accretion disk, single-dot-dashed = SSC, dot-double-dashed = EC (accretion disk), double-dot-dashed = EC (isotropic radiation field).

$L_{\rm BLR}=\tau\,L_{\rm disk}$, and these quantities are related to the energy densities of the respective radiation fields in the co-moving frame of the emission region through (Dermer and Menon, 2009)

$$\frac{u_{\rm ext}}{u_B} = \frac{8\cdot L'_d\cdot\tau\cdot\Gamma^2}{3\cdot B^2\cdot R'^2_{\rm ext}\cdot c} \tag{20}$$

$$\frac{u_{\rm disk}}{u_B} = \frac{6\cdot G\cdot M_{bh}\cdot\dot m\cdot\Gamma^2\cdot 0.023}{B^2\cdot c\cdot R^3_{\rm axis}} \tag{21}$$

We may relate the observed synchrotron peak frequency to the Doppler factor, magnetic field and peak electron energy, assuming that the peak energy corresponds to $\gamma_{\rm min}$. Assuming that SSC scattering is in the Thomson regime, the peak location of the SSC power will then be located at $\nu_{SSC}=\nu_{syn}\cdot\gamma^2_{\rm min}$. Given a constraint on the Doppler factor, this provides estimates for $\gamma_{\rm min}$ and B. Unfortunately, the spectral slope of the synchrotron spectrum is difficult to constrain for 3C273 due to the substantial contribution from the accretion disk in the optical regime, which is masking much of the synchrotron emission.

Within the framework of the observational constraints, the remaining parameters are varied to obtain an acceptable fit to the SED of 3C273. Fig. 1 shows the SED fit obtained, with parameters listed in Table 1. Our fitting procedure is a "fit by eye" method. Due to the considerable number of adjustable parameters not constrained by observations, a detailed χ^2 minimization procedure is infeasible. While our fit parameters might provide a reasonable estimate of the actual physical conditions in the emission region, the lack of a rigorous χ^2 minimization procedure makes an error analysis impractiable. However, since the goal of this paper is the study of light curve features resulting from individual parameter variations, the exact value of any individual parameter is irrelevant for our purpose.

Fig. 1 illustrates that the SED of 3C273 is reproduced quite well with our fit. The optical to near UV radiation is fitted well by a combination of synchrotron and direct accretion disk emission. The value of $B=1.75$ g is consistent typical values (of the order of 1 – a few G) found in the modeling of FSRQs by other authors (e.g., Ghisellini et al., 2011; Böttcher et al., 2013; Dermer et al., 2014). The X-ray spectrum is fitted with a synchrotron self Compton component, and the *Fermi*-LAT data points are fitted with external-Compton radiation, also in agreement with

Table 1
Parameter values used for the equilibrium fit to the SED of 3C273 (see Fig. 1).

Parameter	Value
B	1.75 G
R	7.25×10^{15} cm
η	18.0
Γ	14
$\theta_{\rm obs}$	7.14×10^{-2} rad
$\gamma_{\rm min}$	6.25×10^{2}
$\gamma_{\rm max}$	1.0×10^{5}
q	3.4
$L_{\rm inj}$	5.6×10^{42} erg s^{-1}
$M_{\rm BH}$	$2.6 \times 10^{9}\, M_{\odot}$
$l_{\rm Edd}$	0.395
$R_{\rm axis}$	0.07 pc
$R'_{\rm ext}$	0.73 pc
$u'_{\rm ext}$	6.5×10^{-5} erg cm^{-3}
$T_{\rm BB}$	6000 K
$t_{\rm acc}/t_{\rm esc}$	1.5×10^{-3}

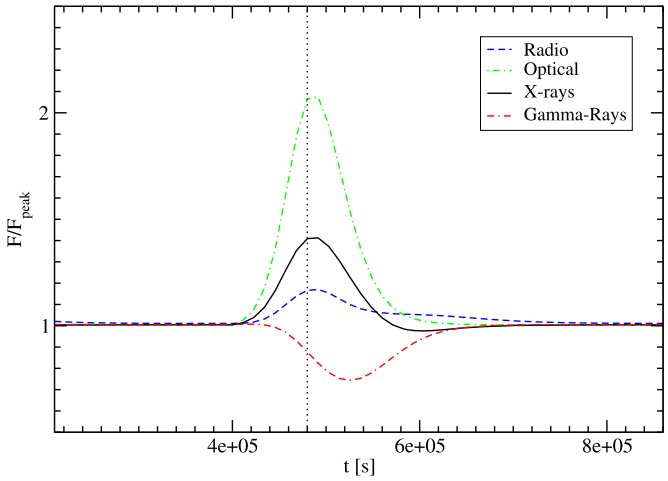

Fig. 2. Normalized light-curves in the radio, optical, X-ray, and γ-ray bandpasses resulting from the magnetic field perturbation (Eq. (22)). The dotted vertical line indicates the value of t_0.

most other modeling works which utilize external Compton scattering to reproduce the γ-ray emission of low-frequency-peaked blazars, as opposed to high frequency BL Lacs that can usually be well represented by pure synchrotron-self-Compton models. In our fit, the external radiation fields is a combination of radiation from the accretion disk and an isotropic external radiation field (representative of the BLR), as suggested by Finke and Dermer (2010) to reproduce the spectral break in the *Fermi*-LAT spectrum of the FSRQ 3C 454.3. The choice of parameters for the isotropic radiation field is consistent with being related to the BLR, given the distance of the emission region from the black hole, $\sim 10^{17}$ cm, the radial extent of the external field, $\sim 10^{18}$ cm, and the blackbody temperature of 6×10^3 K (see, e.g., Böttcher et al., 2013). The distance from the black hole is also consistent with the near-field approximation adopted for the accretion disk radiation field. The radio emission is suppressed due to synchrotron self absorption, which suggests that the extended radio emission is likely due to synchrotron emission of electrons further down the jet.

Our fit employs a moderate diffusive acceleration time scale of $t_{\rm acc} = 6.5 \times 10^3$ s, which is longer than the radiative cooling time scale of electrons at $\gamma_{\rm max}$. Therefore, the influence of Fermi-II acceleration on the presented steady-state fit is negligible. However, as we will see in the next sections, this is no longer the case for the flaring scenarios that we investigate.

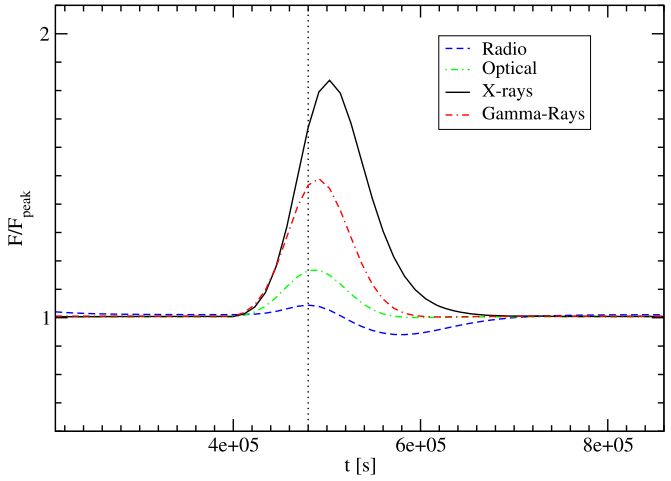

Fig. 3. Normalized light-curves in the radio, optical, X-ray, and γ-ray bandpasses resulting from the injection luminosity perturbation (Eq. (23)). The dotted vertical line indicates the value of t_0.

4. Simulated light-curves

Starting with the steady state model setup for 3C273 as described above, we now investigate the influence of fluctuations of individual parameters on the time-dependent radiative output. After the simulation has reached equilibrium, one of the input parameters (B, $L_{\rm inj}$, or $t_{\rm acc}$) is modified in the form of a Gaussian perturbation in time. From the simulation outputs, we extract light curves in the radio, optical (R-band), X-ray and GeV γ-ray (*Fermi*-LAT) bandpasses. Specifically, we setup the time evolution of the magnetic field perturbation as

$$B(t) = B_0 + K_B \cdot e^{-(t-t_0)^2/2\sigma^2} \tag{22}$$

where $B_0 = 1.75$ G is the equilibrium value for the magnetic field, $K_B = 2$ G parameterizes the amplitude of the perturbation, and t_0 and σ specify the time when the perturbation reaches its maximum and the characteristic time scale of the perturbation, respectively. The chosen perturbation for the injection luminosity has the same functional form,

$$L_{\rm inj}(t) = L_{\rm inj,0} + K_L \cdot e^{-(t-t_0)^2/2\sigma^2} \tag{23}$$

where $L_{\rm inj,0} = 5.6 \times 10^{42}$ erg s^{-1} is the equilibrium injection luminosity and $K_L = 4.8 \times 10^{42}$ erg s^{-1} is the amplitude of the perturbation. The perturbation of the acceleration time scale is chosen in such a way that the acceleration time scale decreases to a minimum during the peak of the perturbation. This is achieved with the following parameterization:

$$t_{\rm acc}(t) = \frac{t_{\rm acc,0}}{1 + K_t \cdot e^{-(t-t_0)^2/2\sigma^2}} \tag{24}$$

where $t_{\rm acc,0}$ is the equilibrium value of the acceleration time scale and $K_t = 17$ characterizes the amplitude of the perturbation. For all three perturbations, we choose a width of $\sigma = 4 \times 10^5$ s, and a peak time of $t_0 = 6.7 \times 10^6$ s, corresponding to approximately 2 and 30 light-crossing time scales through the emission region, respectively, both in the co-moving frame. The light curves (normalized to the respective peak fluxes) are shown in Figs. 2–4.

As expected, the increase in the magnetic field (Fig. 2) causes an increase in the synchrotron flux at all energies (specifically, radio and optical for the case studied here). The associated increase in the synchrotron photon energy density also causes a flare in the SSC-dominated X-ray emission. At the same time, this leads to increased radiative cooling without a change of the external radiation fields and, hence, a dip in the γ-ray light curve. This dip is

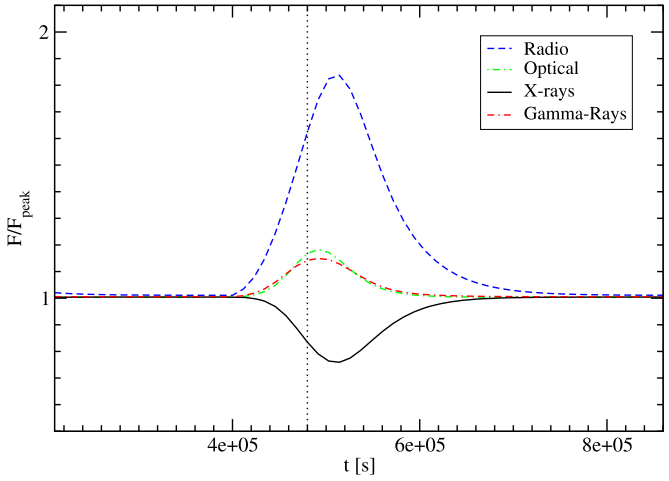

Fig. 4. Normalized light-curves in the radio, optical, X-ray, and γ-ray bandpasses resulting from the acceleration time scale perturbation (Eq. (24)). The dotted vertical line indicates the value of t_0.

Table 2
Simulated light curve parameters for the case of the magnetic field perturbation. Fluxes, f_0 and f_{pk}, are given in units of erg cm^{-2} s^{-1}, while the FWHM and peak time, t_{pk}, are given in units of seconds.

	Radio	R-band	X-rays	γ-rays
f_0	7.5×10^{-16}	2.68×10^{-11}	1.78×10^{-10}	6.85×10^{-10}
f_{pk}	8.71×10^{-16}	5.53×10^{-11}	2.50×10^{10}	5.1×10^{-10}
FWHM	8.36×10^{4}	7.31×10^{4}	7.80×10^{4}	9.57×10^{4}
t_{pk}	4.86×10^{5}	4.87×10^{5}	4.87×10^{5}	5.26×10^{5}

delayed with respect to the maxima in the synchrotron and SSC light curves by approximately the radiative cooling time scale of γ-ray emitting electrons.

A temporarily increased injection luminosity (Fig. 3) initially causes a flare in all bandpasses. However, we find a delayed decrease of the radio flux following an initial, small-amplitude flare. This is explained by an increased density of relatively low-energy electrons, responsible for synchrotron self-absorption at radio wavelengths, delayed by the required radiative cooling time scale for newly injected electrons to reach Lorentz factors of $\lesssim 100$.

A decreasing acceleration time scale (Fig. 4) leads to more efficient acceleration of relativistic particles to higher energies. The electron spectrum becomes harder and extends to higher energies during this perturbation, which shifts all spectral components to higher frequencies. This leads to flaring behavior in the radio, optical, and γ-ray bands. The X-ray flux, however, corresponding to the low-frequency branch of the SSC emission component, decreases due to the shift of the SSC component to higher frequencies. The flare in the radio bandpass is particularly pronounced in this simulation. Keeping in mind that the radio emission is in the optically-thick (to SSA) regime, this can be explained by low-energy electrons being accelerated to higher energies, out of the energy range contributing to synchrotron self-absorption at radio wavelengths, thereby reducing the effective number density of electrons for SSA. Due to the much steeper frequency dependence of the SSA opacity compared to the synchrotron emissivity, the net effect is an increase in the emanating synchrotron flux.

The light curves shown in Figs. 2 to 4 reveal noticeable delays between the light curve features in different frequency bands. Tables 2–4 list the simulated equilibrium fluxes f_0, peak fluxes f_{pk}, FHWM and peak times t_{pk} of the light curves in the four studied frequency bands for the three perturbations investigated here. The fluxes, f_0 and f_{pk}, are given in units of erg cm^{-2} s^{-1}, while the FWHM and peak time, t_{pk}, is given in units of seconds.

Table 3
Simulated light curve parameters for the case of the injection luminosity perturbation. Fluxes, f_0 and f_{pk}, are given in units of erg cm^{-2} s^{-1}, while the FWHM and peak time, t_{pk}, are given in units of seconds.

	Radio	R-band	X-rays	γ-rays
f_0	7.5×10^{-16}	2.68×10^{-11}	1.78×10^{-10}	6.85×10^{-10}
f_{pk}	7.03×10^{-16}	3.13×10^{-11}	3.26×10^{10}	1.01×10^{-9}
FWHM	9.43×10^{4}	6.45×10^{4}	8.51×10^{4}	7.81×10^{4}
t_{pk}	5.74×10^{5}	4.87×10^{5}	5.03×10^{5}	4.89×10^{5}

Table 4
Simulated light curve parameters for the case of the acceleration timescale perturbation. Fluxes, f_0 and f_{pk}, are given in units of erg cm^{-2} s^{-1}, while the FWHM and peak time, t_{pk}, are given in units of seconds.

	Radio	R-band	X-rays	γ-rays
f_0	7.5×10^{-16}	2.68×10^{-11}	1.78×10^{-10}	6.85×10^{-10}
f_{pk}	1.36×10^{-15}	3.16×10^{-11}	1.35×10^{-10}	7.86×10^{-10}
FWHM	1.04×10^{5}	7.37×10^{4}	9.01×10^{4}	9.08×10^{4}
t_0	5.11×10^{5}	4.87×10^{5}	5.10×10^{5}	4.90×10^{5}

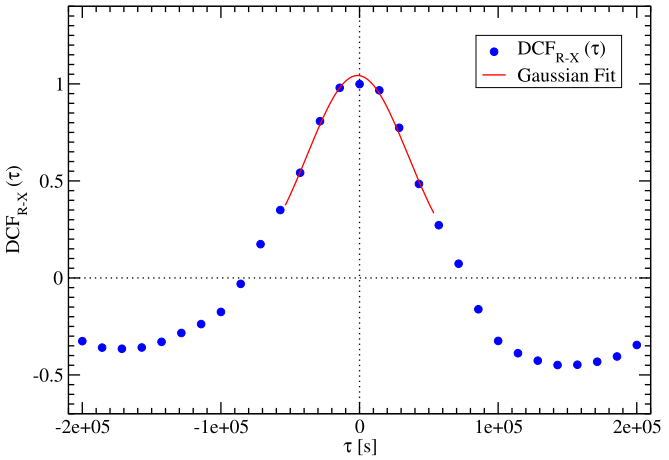

Fig. 5. Discrete correlation function between the optical (R-band) and X-ray bandpasses for the magnetic field perturbation case, along with a Gaussian fit to the DCF.

The predicted anti-correlation between the X-ray fluxes and the radio, optical, and γ-ray fluxes found for the case of the acceleration timescale perturbation, is a particularly interesting feature. These correlations and anti-correlations could represent a tell-tale signature of flaring activity caused by a temporary increase of the efficiency of Fermi II acceleration in the emission region.

5. Discrete correlation analysis of light-curve bandpasses

In order to be able to directly compare our predictions to light curve features extracted from observational data, we apply a discrete correlation function (DCF) analysis (Edelson and Krolik, 1988) between the light curves at the various bandpasses investigated here, as is routinely done for data from flux-monitoring campaigns on blazars to study correlations/anti-correlation and time lags between different frequency bands. We arbitrarily assign a relative error of 1% of the flux values to any simulated light curve point in order to be able to apply a χ^2 minimization technique to fit a phenomenological Gaussian function to the obtained DCFs. For comparison with observational data, which typically have the most complete temporal light curve coverage in the optical and γ-ray (*Fermi*-LAT) — and occasionally also X-ray — bands, we here focus on the cross correlations between the optical and the X-ray and γ-ray bands. The resulting DCFs are shown in Figs. 5 to 10.

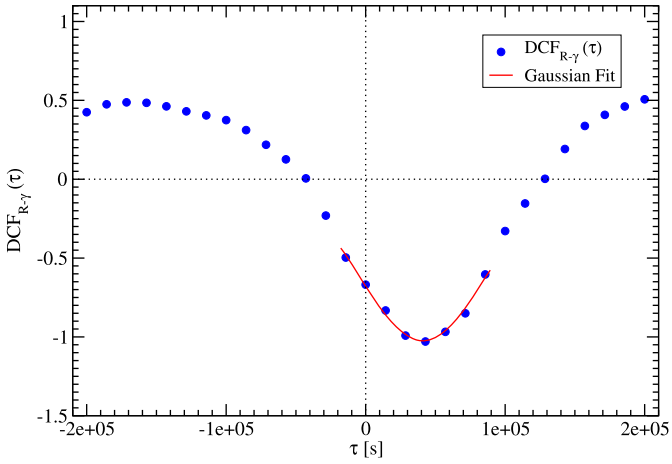

Fig. 6. Discrete correlation function between the optical (R-band) and γ-ray bandpasses for the magnetic field perturbation case, along with a Gaussian fit to the DCF.

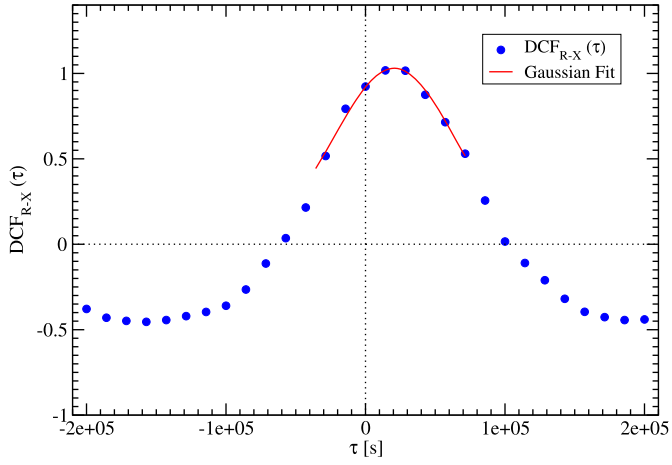

Fig. 7. Discrete correlation function between the optical (R-band) and X-ray bandpasses for the injection luminosity perturbation case, along with a Gaussian fit to the DCF.

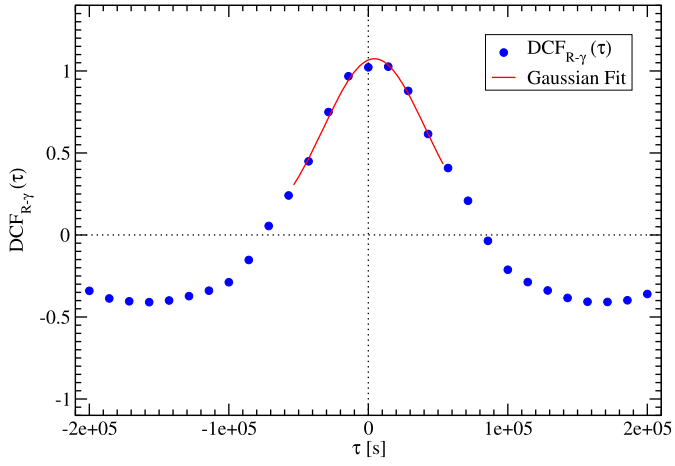

Fig. 8. Discrete correlation function between the optical (R-band) and γ-ray bandpasses for the injection luminosity perturbation case, along with a Gaussian fit to the DCF.

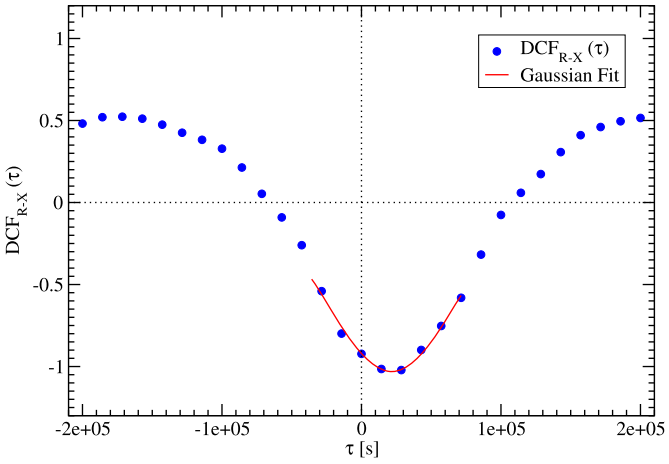

Fig. 9. Discrete correlation function between the optical (R-band) and X-ray bandpasses for the acceleration time scale perturbation case, along with a Gaussian fit to the DCF.

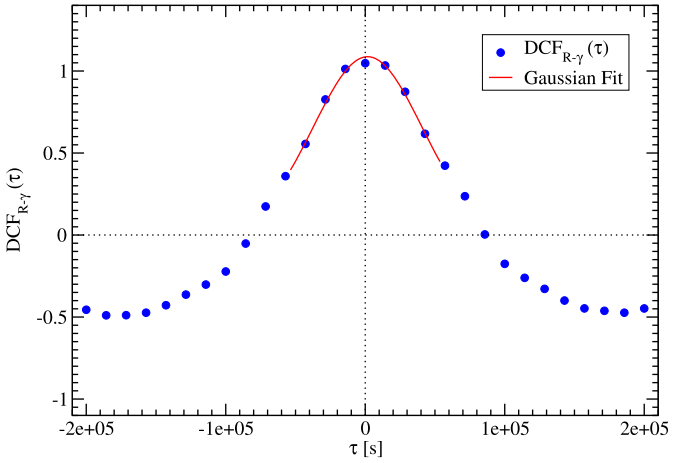

Fig. 10. Discrete correlation function between the optical (R-band) and γ-ray bandpasses for the acceleration time scale perturbation case, along with a Gaussian fit to the DCF.

Table 5
Best-fit DCF correlation strengths and time lags from the Gaussian fits to the discrete correlation functions.

	F_1	σ [s]	τ_{pk} [s]	Fig.
$R-X:B$	1.08	$(4.97 \pm 0.48) \times 10^4$	$(-2.37 \pm 4.84) \times 10^3$	Fig. 5
$R-\gamma:B$	−1.04	$(5.96 \pm 0.57) \times 10^4$	$(5.96 \pm 0.57) \times 10^4$	Fig. 6
$R-X:L_{\rm inj}$	1.06	$(5.62 \pm 0.58) \times 10^4$	$(1.94 \pm 0.51) \times 10^4$	Fig. 7
$R-\gamma:L_{\rm inj}$	1.11	$(4.97 \pm 0.49) \times 10^4$	$(4.96 \pm 4.92) \times 10^3$	Fig. 8
$R-X:t_{\rm acc}$	−1.05	$(5.97 \pm 0.56) \times 10^4$	$(3.22 \pm 0.54) \times 10^4$	Fig. 9
$R-\gamma:t_{\rm acc}$	1.13	$(5.39 \pm 0.49) \times 10^4$	$(8.02 \pm 5.16) \times 10^3$	Fig. 10

The DCF reveals correlations/anti-correlations between two light curves, with a peak value of ± 1 indicating a perfect correlation/anti-correlation, respectively. The time lag τ at which the peak occurs, indicates a time lag between the variability patterns in the two light curves. In all cases, the DCF results shown in Figs. 5–10 confirm the correlation and time lag results apparent from Figs. 2–4 and Tables 2–4.

For a more rigorous analysis of the time lags and their errors, we performed a Gaussian fit of the form

$$DCF(\tau) = F_1 \cdot e^{-(\tau-\tau_{pk})^2/2\sigma^2} \tag{25}$$

to each of the discrete correlation functions around the peaks/troughs of the DCFs. This was done by rigorous χ^2 minimization.

The minimization produces the best fit parameters for the normalization, F_1, the location of the peak time delay, τ_{pk}, and the standard deviation of the peak, σ. The best fit parameters are listed in Table 5. Within error bars, the time lags determined from the DCFs agree well with those extracted from inspection of the light curves (Tables 2–4).

6. Results and discussion

In this paper, we describe the development of a time-dependent model for the broadband emission from blazars, incorporating Fermi II acceleration in the time evolution of the electron distribution, as well as internal (SSC) and external (EC) target photon fields for Compton scattering, using the full Klein–Nishina cross section. The use of a power law distribution for the electron injection spectrum is motivated by the physical picture of Fermi I acceleration providing the effective injection mechanism. We consider two external radiation fields, namely the accretion disk and a second radiation field that is approximated as being isotropic in the AGN rest frame, representative of either the BLR or of IR emission from a dust torus. The code was used for a generic study of the influence of a diffusive acceleration process on the equilibrium electron distribution and SEDs from blazars, and of the multi-wavelength radiative signatures of fluctuations of individual model parameters, including the Fermi-II acceleration efficiency. The choice of baseline parameters was guided by a fit to the time-averaged SED of the FSRQ 3C273, with our model simulation in a steady-state. Our study is therefore representative of features expected for FSRQs or other low-frequency peaked blazars. We then investigated the potentially observable signatures of flaring activity caused by short-term fluctuations of (a) the magnetic field, (b) the electron injection luminosity, and (c) the acceleration time scale. A discrete correlation function analysis was performed on the light curves simulated for the different flaring scenarios, at radio, optical, X-ray, and γ-ray frequencies to quantify the predicted strengths of cross-band correlations and associated time lags.

We found that magnetic field fluctuations lead to correlated radio, optical, and X-ray flaring, but an anti-correlation of these three bands with the γ-ray emission, with a time lag of up to several hours, due to increased synchrotron and SSC cooling of relativistic electrons. Flaring activity caused by fluctuations of the injection luminosity lead to correlated variability in all wavelength ranges, with a time lag of a few hours between the optical and X-ray flares, associated with the cooling time scale of electrons to reach low energies contributing to SSC X-ray emission. In this scenario, the radio emission shows a delayed drop in flux, due to the increase of the synchrotron self absorption caused by the increased number of low-energy electrons. A temporary shortening of the acceleration time scale intensified both the synchrotron and Compton emission and leads to a shift of both components to higher frequencies due to the acceleration of electrons to higher energies. Apart from correlated flaring activity at optical and γ-ray frequencies, this has interesting consequences at X-rays and radio wavelengths: The shift of the SSC emission to higher frequencies leads to a decrease of the (SSC-dominated) X-ray flux and therefore an anti-correlation between the optical/γ-ray and X-ray fluxes with time delays of a few hours. At the same time, the more efficient electron acceleration reduces the number of low-energy electrons responsible for synchrotron self-absorption at radio wavelengths and therefore leads to a radio flare correlated with the optical/γ-ray activity.

Recent multi-wavelength observations of FSRQs have shown correlations between different wavelength bands that can be attributed to flares simulated in this paper. Multi-wavelength observations of the FSRQ 3C 454.3 from August–December 2008 have shown pronounced flaring activity in the IR, UV, X-ray and γ-ray bands with correlations for all bands except the X-rays (Bonning et al., 2009). These correlations are consistent with a model in which a change in the injection luminosity of higher energy electrons takes place and interacts with external photons, causing the flaring observed in the γ-rays (Bonning et al., 2009). The much longer cooling time of the low-energy electrons responsible for the X-ray emission leads to much delayed variability, on much longer time scales compared to the optical and γ-ray bands, which might be washed out by super-imposed longer-term variability. Correlated multi-wavelength campaigns have also been done on the FSRQ 3C273 that reveal a correlation between the IR and X-ray bands, with time lags on the order of a few hours (McHardy et al., 2007). This is consistent with the results presented here and supports the notion that the X-ray emission is dominated by synchrotron self Compton radiation (McHardy et al., 2007).

We point out that our ad-hoc choice of Gaussian perturbations to key parameters only serves to study generic features of such changes. As has become obvious, the salient predictions concerning correlations/anti-correlations and time lags result from the microphysical processes of electron acceleration and cooling and are only weakly dependent on the exact time profile of the perturbation.

Acknowledgments

We thank the anonymous referee for a quick review and a constructive report which helped to improve the manuscript. This work was funded by NASA through Astrophysics Data Analysis Program grant NNX12AE43G. The work of M.B. is supported through the South African Research Chair Initiative of the National Research Foundation and the Department of Science and Technology of South Africa, under SARChI Chair grant No. 64789.

References

Abdo, A.A., et al., 2010. ApJ 716, 30.
Asano, K., Takahara, F., et al., 2013. ApJ 780, 64.
Becker, P., Dermer, C., 2006. ApJ 647, 539.
Blandford, R.D., Levinson, A., 1995. ApJ 441, 79.
Blazejowski, M., et al., 2000. ApJ 545, 107.
Bonning, E.W., Bailyn, C., et al., 2009. ApJ 697, 81B.
Böttcher, M., Mause, H., et al., 1997. A&A 324, 395.
Böttcher, M., Schlickeiser, R., 1997. A&A 325, 866.
Böttcher, M., 2007. ApSS 309, 95.
Böttcher, M., Harris, D.E., Krawczynski, H., 2012. Relativistic Jets from Active Galactic Nuclei. WILEY-VCH Verlag GmBH & Co.
Böttcher, M., Reimer, A., et al., 2013. ApJ 768, 54.
Cerruti, M., Dermer, C.D., Lott, B., Boisson, C., Zech, A., 2013. ApJ 771, L4.
Dermer, C.D., Schlickeiser, R., Mastichiadis, A., 1992. A&A 256, L27.
Dermer, C.D., Schlickeiser, R., 1993. ApJ 416, 458.
Dermer, C.D., Menon, G., 2009. High Energy Radiation from Black Holes. Princeton University Press.
Dermer, C.D., Cerruti, M., Lott, B., Boisson, C., Zech, A., 2014. ApJ 782, 82.
Edelson, R.A., Krolik, J.H., 1988. ApJ 333, 646.
Finke, J.D., Dermer, C.D., 2010. ApJ 714, L303.
Ghisellini, G., Tavecchio, F., Foshini, L., Ghirlanda, G., 2011. MNRAS 414, 2674.
Jones, F.C., 1968. Phys. Rev. 167, 1159.
Lefa, E., Rieger, F.M., et al., 2011. ApJ 760, 64.
Mannheim, K., Biermann, P.L., 1992. A&A 253, L21.
Massaro, E., Perri, M., et al., 2006a. A&A 413, 489.
Massaro, E., Tramacere, A., et al., 2006b. A&A 448, 861.
Mastichiadis, A., Kirk, J.G., 1995. A&A 295, 613.
Mastichiadis, A., Kirk, J.G., 2005. A&A 433, 765.
McHardy, I., Lawson, A., et al., 2007. MNRAS 375, 1521M.
Mücke, A., Protheroe, R.J., 2001. APh 15, 121.
Mücke, A., Protheroe, R.J., Engel, R., Rachen, J.P., Stanev, T., 2003. APh 18, 593.
Rani, B., Gupta, A., et al., 2011. MNRAS 417, 1181.
Schlickeiser, R., 1984a. A&A 136, 227.
Schlickeiser, R., 1984b. A&A 143, 431.
Shakura, N.I., Sunyaev, R.A., 1973. A&A 24, 337.
Sikora, M., Begelman, M., Rees, M., 1994. ApJ 421, 153.
Stawarz, L., Petrosian, V., 2008. ApJ 681, 1725.
Tramacere, A., Massaro, E., et al., 2011. ApJ 739, 66.